

Interfacial engineering of $\text{Co}_{5.47}\text{N}/\text{Mo}_5\text{N}_6$ nanosheets with rich active sites synergistically accelerates water dissociation kinetics for Pt-like hydrogen evolution

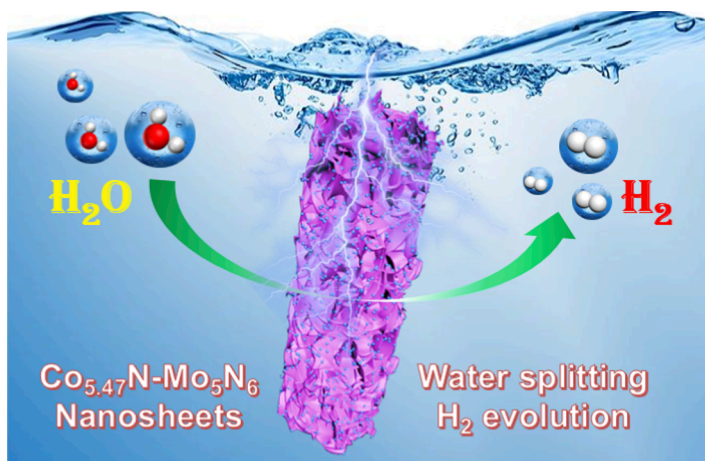
Yan Hu^{a,b,1}, Zhiyang Huang^{a,1}, Qing Zhang^b, Tayirjan Taylor Isimjan^a, Youqi Chu^b, Yongbiao Mu^b, Baoxin Wu^b, Zebing Huang^b, Xiulin Yang^{a,*}, Lin Zeng^{b,*}

^a Guangxi Key Laboratory of Low Carbon Energy Materials, School of Chemistry and Pharmaceutical Sciences, Guangxi Normal University, Guilin 541004, China

^b Department of Mechanical and Energy Engineering, Southern University of Science and Technology, Shenzhen 518055, China

GRAPHICAL ABSTRACT

A heterostructured $\text{Co}_{5.47}\text{N}/\text{Mo}_5\text{N}_6$ catalyst on carbon cloth is created through a dip-etching and vapor nitridation process. It showcases Pt-like HER activity, reaching a potential of 44 mV at 10 mA cm^{-2} . When used as a cathode in high-current overall water splitting, it requires only a cell voltage of 1.81 V to reach 200 mA cm^{-2} , making it a promising candidate for industrial use. The catalyst's unique nanosheet structure with a rough surface and the synergistic effect of $\text{Co}_{5.47}\text{N}$ and Mo_5N_6 contribute to its enhanced HER performance.



ARTICLE INFO

Keywords:

$\text{Co}_{5.47}\text{N}/\text{Mo}_5\text{N}_6$
Rough nanosheet
Synergistic effect

ABSTRACT

The development of highly efficient hydrogen evolution electrocatalysts with platinum-like activity requires precise control of active sites through interface engineering strategies. In this study, a heterostructured $\text{Co}_{5.47}\text{N}/\text{Mo}_5\text{N}_6$ catalyst (CoMoN_x) on carbon cloth (CC) was synthesized using a combination of dip-etching and vapor nitridation methods. The rough nanosheet surface of the catalyst with uniformly distributed elements exposes a

* Corresponding authors.

E-mail addresses: xlyang@gxnu.edu.cn (X. Yang), zengl3@sustech.edu.cn (L. Zeng).

¹ These authors contributed equally to this work.

<https://doi.org/10.1016/j.jcis.2023.04.028>

Received 8 February 2023; Received in revised form 14 March 2023; Accepted 7 April 2023

Available online 8 April 2023

0021-9797/© 2023 Elsevier Inc. All rights reserved.

Hydrogen evolution
Density functional theory

large active surface area and provides abundant interface sites that serve as additional active sites. The CoMoN_x was found to exhibit exceptional hydrogen evolution reaction (HER) activity with a low overpotential of 44 mV at 10 mA cm⁻² and exceptional stability of 100 h in 1.0 M KOH. The CoMoN_x⁽⁻⁾||RuO₂⁽⁺⁾ system requires only 1.81 V cell voltage to reach a current density of 200 mA cm⁻², surpassing the majority of previously reported electrolyzers. Density functional theory (DFT) calculations reveal that the strong synergy between Co_{5,47}N and Mo₅N₆ at the interface can significantly reduce the water dissociation energy barrier, thereby improving the kinetics of hydrogen evolution. Furthermore, the rough nanosheet architecture of the CoMoN_x catalyst with abundant interstitial spaces and multi-channels enhances charge transport and reaction intermediate transportation, synergistically improving the performance of the HER for water splitting.

1. Introduction

The drive to decarbonize in response to climate change is increasingly motivating the widespread deployment of hydrogen energy. Low-carbon, clean hydrogen is seen as a key factor in achieving carbon neutrality [1,2]. Renewable hydrogen is typically produced through an alkaline water electrolysis process [3,4], but the slow kinetics of the hydrogen evolution reaction (HER) in alkaline media results in low electrolysis efficiency [5]. Platinum-based materials are highly effective but their scarcity and high cost limit their use [6,7]. Therefore, developing non-noble metal HER electrocatalysts with abundant reserves and platinum-like activity is crucial for advancing the hydrogen economy, but remains challenging due to limitations in activity and durability [8]. To overcome these limitations and advance the practical application of hydrogen energy, the development of HER electrocatalysts with high activity and stability through novel design methods is necessary.

Recently, the development of efficient non-precious metal electrocatalysts for HER has been a topic of significant interest [9]. Researchers have focused on enhancing the catalytic activity and durability of these catalysts through various strategies such as heteroatom doping [10], strain engineering [11], and interface engineering [12]. Despite these advances, a major challenge in the use of high-performance HER catalysts is their poor interfacial stability [13,14]. During stability tests, the electrode surface often experiences a significant amount of mechanical resistance, causing the catalyst to fall off the electrode and making it difficult to maintain stability [14]. To address this challenge, researchers have explored in-situ assembly of the catalysts on high surface area, conductive substrates such as nickel foam, carbon cloth, and carbon paper [15,16]. This approach can effectively increase the adhesion between the catalyst and substrate and reduce the mechanical resistance during electrocatalysis, leading to improved stability of the electrode.

Another promising strategy is the construction of functional nanocomposite heterostructures, as they offer great potential for regulating the physicochemical properties of the composites and enhancing the performance of hybrid electrocatalysts [17]. Heterogeneous interfaces play a crucial role in this process, as they allow for synergistic effects between different components, favorable electronic structure, and better chemical environments at the interface, leading to an increased exposure of active sites and enhanced intrinsic activity and stability of the catalytic sites for the HER [17,18]. Transition metal nitrides are particularly attractive due to their excellent electrical conductivity and corrosion resistance [19]. For instance, Jiao et al. demonstrated that Co-Mo₅N₆ can manipulate the electron redistribution between the nitrogen-rich phase and cobalt to lower the dissociation energy barrier and optimize the intermediate H* adsorption, thereby improving HER activity [20]. Similarly, Jiang et al. reported that the Co/CoMoN/NF heterostructures exhibited excellent HER activity in 1.0 M KOH solution with a low overpotential of 173 mV at 100 mA cm⁻² [21]. The improved performance was attributed to the role of cobalt sites with a low-valent state as efficient water dissociation promoters, while the CoMoN substrate reduced hydrogen adsorption energy, thereby enhancing the HER activity.

The present study describes the preparation of heterostructured CoMoN_x nanosheets as a highly efficient and stable HER electrocatalyst.

The catalyst was formed in situ on a carbon cloth substrate via a facile dip-etching method and vapor nitridation treatment. Microstructural and chemical analysis confirmed the presence of Co_{5,47}N and Mo₅N₆ crystals, as well as heterogeneous interfaces. Electrochemical evaluations showed that the CoMoN_x catalyst exhibited exceptional HER activity (44 mV at 10 mA cm⁻²) and stability (100 h in an alkaline medium). Additionally, the catalyst demonstrated high specific and intrinsic catalytic activity, outperforming the commercial Pt/C catalyst in terms of cell voltage required to reach a current density of 200 mA cm⁻² (1.81 V for CoMoN_x compared to 1.86 V for Pt/C). Density functional theory calculations revealed that the heterostructured interface of Co_{5,47}N and Mo₅N₆ lowered the energy barrier for water dissociation, promoting the formation of H* and boosting the HER activity.

2. Experimental section

2.1. Chemicals and materials

Cobalt nitrate hexahydrate (Co(NO₃)₂·6H₂O, 99.0%), 2-methylimidazole and RuCl₃ were purchased from Shanghai Aladdin Biochemical Technology Co., Ltd. Sodium molybdate dehydrate (Na₂MoO₄·2H₂O, 99.0%) was acquired from Xilong Science Co., Ltd. Commercial Pt/C (20 wt% for platinum) was purchased from Alfa Aesar. Carbon cloth (CC) was obtained from Suzhou Sinero Technology Co., Ltd. These chemicals were analytical grade and utilized without additional purification. Deionized (DI) water (resistivity ≥ 18.2 MΩ, Millipore Milli-Q) was used for the preparation of the electrolytes.

2.2. Synthesis of ZIF-67/CC

All chemicals used were of analytical grade and detailed information can be found in the [Supporting Information](#). The synthesis of ZIF-67 nanosheets on carbon cloth (CC) was performed following a modified version of a previously reported method [22]. The CC was first cleaned ultrasonically in 0.5 M H₂SO₄, DI water, and ethanol for 15 min each. Then, 1.6 mmol of Co(NO₃)₂·6H₂O and 8 mmol of 2-methylimidazole were dissolved in 20 mL of DI water and mixed under stirring. The pretreated CC was then placed in the mixture for 6 h. Finally, the resulting ZIF-67 modified CC (ZIF-67/CC) was taken out, washed with DI water, and dried naturally.

2.3. Synthesis of CoMo(OH)_x/CC

The preparation of CoMo(OH)_x nanosheets on carbon cloth (CC) was achieved through impregnation. 300 mg of Na₂MoO₄·2H₂O was dissolved in 20 mL of DI water and stirred continuously for 30 min. The ZIF-67/CC precursor was then immersed in the solution and stirred at room temperature for 4 h. After multiple washes and air-drying, the final product was named as CoMo(OH)_x/CC.

2.4. Synthesis of CoMoN_x/CC

The CoMo(OH)_x/CC was subjected to annealing in a tube furnace at 420 °C for 5 h with a heating rate of 5 °C per minute in a high purity NH₃

atmosphere (99.99%). The resulting sample was referred to as CoMoN_x/CC. For comparison, the Co_{5.47}N/CC was synthesized using the same nitriding procedure with the ZIF-67/CC precursor.

2.5. Synthesis of RuO₂

RuO₂ powder was synthesized by directly calcining RuCl₃ in the air at 400 °C. The corresponding XRD pattern was indexed to RuO₂ (JCPDS: 40–1290), indicating that RuO₂ was successfully prepared. Besides, The SEM image showed that RuO₂ existed in the form of particles (Fig. S2).

2.6. Electrochemical measurements

The hydrogen evolution reaction (HER) activity was evaluated using a Biologic VMP3 electrochemical workstation with a standard three-electrode system in 1.0 M KOH. The as-prepared catalyst, graphite plate, and saturated calomel electrode (SCE) were used as the working electrode, counter electrode, and reference electrode, respectively. The HER activity was determined through cyclic voltammetry (CV) at a sweep rate of 10 mV s⁻¹ and a potential range of -0.9 to -1.5 V (vs. SCE). The polarization curves were obtained through linear sweep voltammetry (LSV) with a scan rate of 1 mV s⁻¹. The potential of the reversible hydrogen electrode (RHE) was calibrated through the equation (Fig. S1) [23]:

$$E(\text{RHE}) = E(\text{SCE}) + 0.241 \text{ V} + 0.059 \times \text{pH}(\text{V vs. RHE}) \quad (1)$$

The electrochemical impedance spectroscopy (EIS) was performed near the onset potential in the frequency range from 200 kHz to 10 mHz. The electrochemically active surface area (ECSA) was estimated by measuring the electrochemical double-layer capacitance (C_{dl}) through CV curves within a non-faradaic interval (-0.9 to -1.0 V) at various scanning rates (10, 20, 40, 60, 80 and 100 mV s⁻¹). The overall water splitting was tested using a two-electrode system with a voltage range of 0 – 2.0 V and a scan rate of 5 mV s⁻¹ in 1.0 M KOH.

2.7. Material characterizations

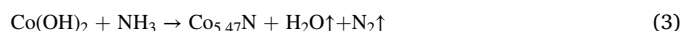
Morphologies and microstructures of the designed materials were

characterized by scanning electron microscopy (SEM, Quanta FEG 200, Holland) and transmission electron microscopy (TEM, JEOL, JEM-2100F). The electron energy loss (EELS) was acquired by a double spherical aberration-corrected transmission electron microscopy (FEI Titan Themis G2). X-ray powder diffraction (XRD) was investigated by a D/Max 2500 V PC with Cu K α radiation. The chemical states of the catalysts were analyzed by X-ray photoelectron spectroscopy (XPS, model: JPS-9010 TR Photoelectron Spectrometer, Japan). The metal contents of the catalysts were determined by inductively coupled plasma-atomic emission spectrometry (ICP-AES, IRIS Intrepid II XSP). The specific surface area and pore size distribution were calculated according to the Brunauer-Emmett-Teller (BET, 3H-2000PS4) and Barrett-Joyner-Halenda (BJH) methods, respectively. Multiple experiments were conducted using BET, BJH and ICP-AES to ensure the accuracy and repeatability of the data.

3. Results and discussion

3.1. Synthesis strategy and structural analysis

The CoMoN_x composite was prepared by a dip-etching and vapor nitridation treatment as illustrated in Fig. 1a. The process started with the growth of purple ZIF-67 precursor (Co(NO₃)₂ as metal source, 2-methylimidazole (2-MIM) as organic ligand) on CC using the impregnation method. The purple ZIF-67/CC precursor was then immersed in Na₂MoO₄ solution to produce peacock blue CoMo(OH)_x nanosheets through etching. The ZIF-67 was unstable in water and etched to release Co²⁺ ions. Since the aqueous solution Na₂MoO₄ was weakly alkaline, these ions undergone a series of complex reactions with hydroxide ions to form corresponding hydroxides [24]. Subsequently, The CoMo(OH)_x was further nitrided under NH₃ atmosphere at 420 °C to generate the CoMoN_x composite (Fig. S3). The possible reactions can be expressed as follows [25,26]:



The phase and chemical composition of the samples were analyzed using X-ray diffraction (XRD). The XRD pattern of the as-prepared ZIF-

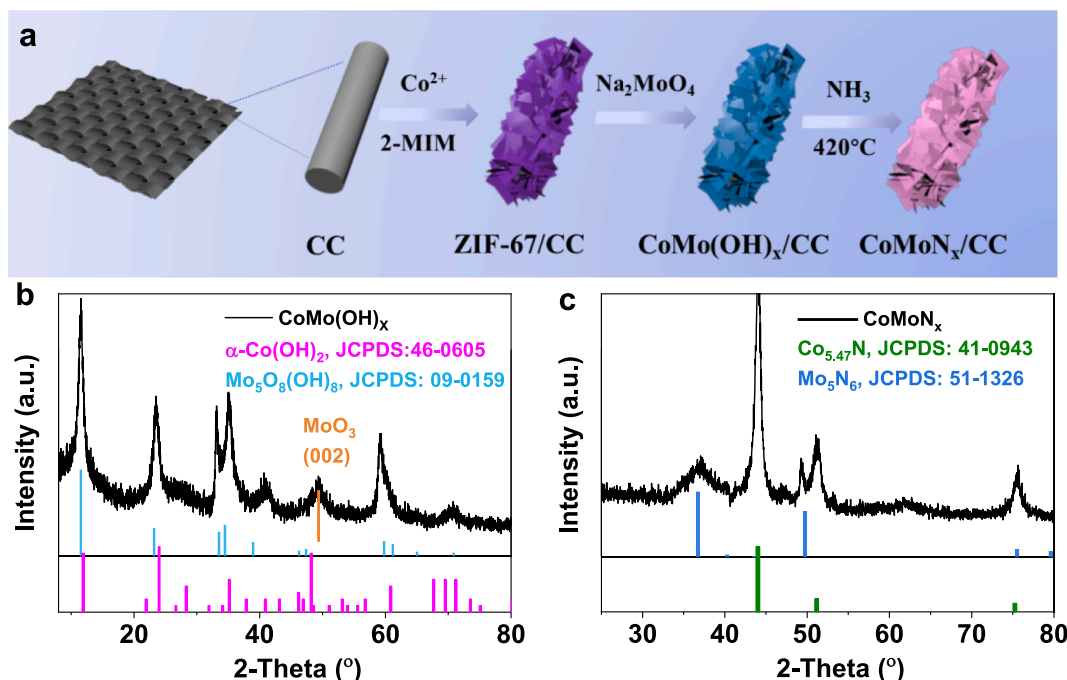


Fig. 1. (a) Schematic illustration of the synthesis process of CoMoN_x. XRD patterns of (b) CoMo(OH)_x and (c) CoMoN_x.

67/CC is shown in Fig. S4a, while the $\text{CoMo}(\text{OH})_x$ etched by Na_2MoO_4 solution exhibits a mixed phase of $\alpha\text{-Co}(\text{OH})_2$ (JCPDS: 46–0605) [27], $\text{Mo}_5\text{O}_8(\text{OH})_8$ (JCPDS: 09–0159), and a small amount of MoO_3 (Fig. 1b). The diffraction peaks of CoMoN_x correspond well to Mo_5N_6 (JCPDS: 51–1326) [25] and $\text{Co}_{5.47}\text{N}$ (JCPDS: 41–0943) phases [28] (Fig. 1c), indicating that CoMoN_x is composed of Mo_5N_6 and $\text{Co}_{5.47}\text{N}$. As a comparison, ZIF-67/CC was successfully converted to $\text{Co}_{5.47}\text{N}/\text{CC}$ after heat treatment in ammonia atmosphere (Fig. S4b) [28].

Scanning electron microscopy (SEM) was used to study the morphologies of ZIF-67/CC, $\text{CoMo}(\text{OH})_x/\text{CC}$, and CoMoN_x/CC . The results showed that ZIF-67 nanosheets (approx. 20 nm thick) were densely packed and smooth on the CC substrate (Fig. S5a). $\text{CoMo}(\text{OH})_x$ nanosheets (ca. 7 nm) retained their nanosheet array structure after nitridation under NH_3 atmosphere (Fig. S5b), while the surface of CoMoN_x/CC became rough with small nanoparticles (Fig. 2a–b) [21].

The microstructure of CoMoN_x nanosheets was further analyzed by transmission electron microscopy (TEM). As illustrated in Fig. 2c, the CoMoN_x nanosheets displayed a porous structure that could expose abundant active sites and facilitate charge transport, improving electrochemical performance sequentially [29]. As shown in the high-resolution HRTEM images (Fig. 2d), the heterostructure between $\text{Co}_{5.47}\text{N}$ and Mo_5N_6 was established. In addition, as marked by the yellow dotted line in Fig. 2d, there are obvious interpenetrating connections between the lattice atoms of $\text{Co}_{5.47}\text{N}$ and Mo_5N_6 , indicating that the two domains are well coupled at the interface. The inverse Fast

Fourier transform (IFFT) images showed that the lattice planes of (111) for $\text{Co}_{5.47}\text{N}$ and (110) for Mo_5N_6 are well exposed in the heterostructure (Fig. 2e–f). Interestingly, the apparent grain boundaries at high magnification were not reflected in the low-resolution elemental mapping, which was consistent with other reports [30,31]. Besides, the Co, Mo and N were detected in the CoMoN_x domains from the high-angle annular dark-field scanning TEM (HAADF-STEM)-energy dispersive X-ray mapping images (Fig. 2g). The electron energy loss spectroscopy (EELS) line scanning of testing area (Fig. 2h) was shown in Fig. 2i–j. The EELS spectra presented a Co-L peak (around 779 and 794 eV), Mo-N peak (around 62 eV) and N-K peak (around 401 eV), which verified the even distribution of Co, Mo and N on the surface of CoMoN_x . Subsequently, the CoMoN_x sample was characterized using an N_2 adsorption–desorption isotherm to determine specific surface area and pore size. As shown in Fig. 2k, the Brunauer-Emmett-Teller (BET) specific surface area and average pore diameter of CoMoN_x were $48.0 \text{ m}^2 \text{ g}^{-1}$ and 12.8 nm, respectively. The high specific surface area of CoMoN_x could be attributed to the formation of abundant mesopores after nitridation [32]. Similar BET results have been reported in self-supported catalysts by many recent works [30,33–35].

3.2. Chemical state analysis

The elemental composition and surface chemical states of catalysts were investigated by X-ray photoelectron spectroscopy (XPS). In

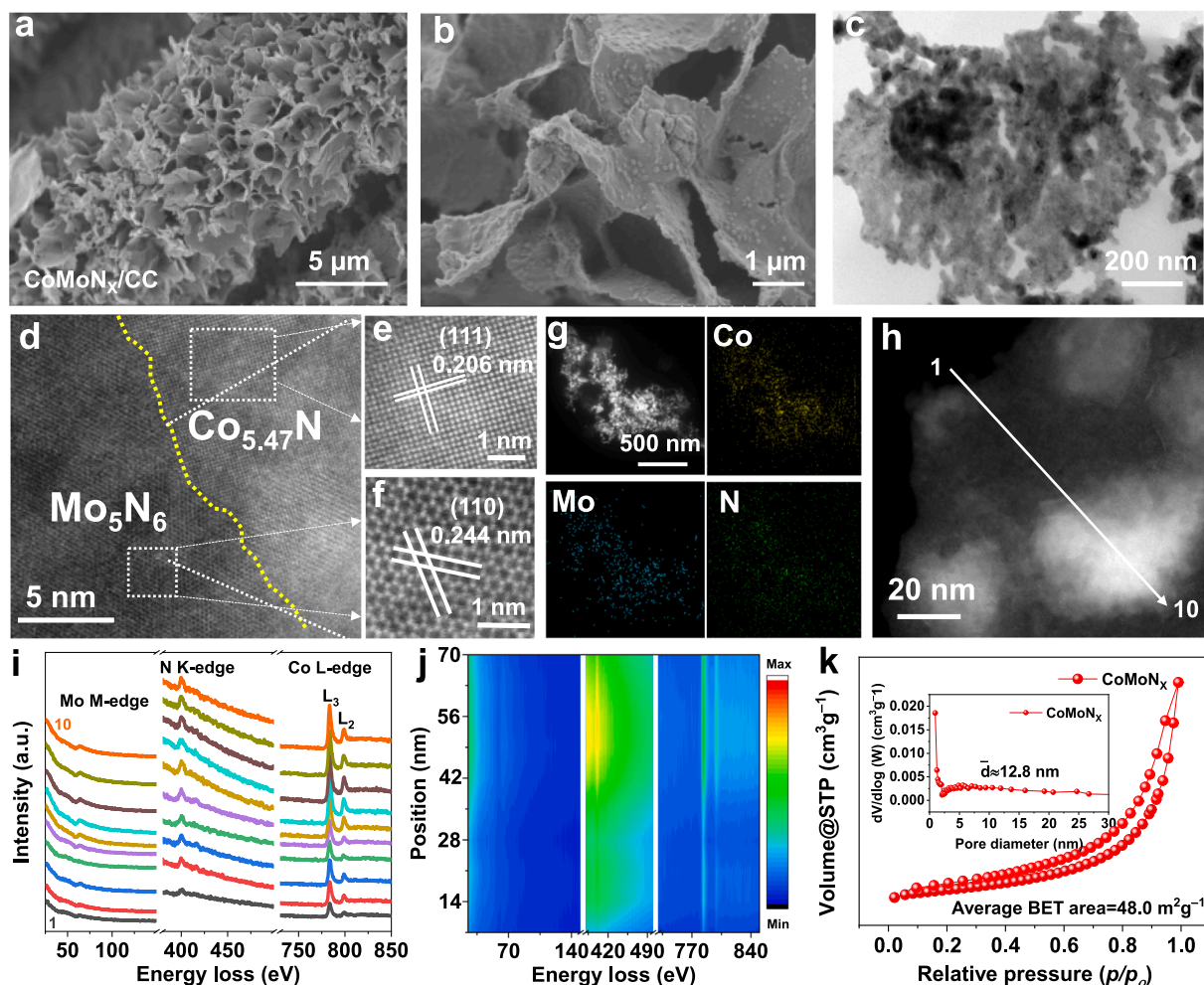


Fig. 2. (a–b) SEM images of CoMoN_x/CC . (c) TEM image of CoMoN_x . (d) HRTEM image of CoMoN_x . IFFT images of (e) $\text{Co}_{5.47}\text{N}$ and (f) Mo_5N_6 . (g) HAADF and corresponding elemental mappings of CoMoN_x (color online). (h) High-resolution STEM image showing the EELS scanning pathway. (i–j) EELS spectra of Co L-edge, Mo M-edge and N K-edge, respectively. (k) Nitrogen adsorption–desorption isotherms with inset pore size distribution of CoMoN_x .

Fig. S6a, the XPS survey spectra showed the presence of Co, Mo, O and N elements in CoMoN_x. The high-resolution C 1 s spectrum of CoMoN_x was assigned to C=C (284.0 eV), C–C (284.8 eV), C–O (286.0 eV) and C=O (288.5 eV) (Fig. S6b) [36]. For Co 2p spectra (Fig. 3a), the Co 2p_{3/2} peaks with binding energies at 779.9 and 781.6 eV correspond to Co³⁺ and Co²⁺, respectively [37,38]. Unlike the CoMo(OH)_x, the peak at 778.0 eV for Co 2p_{3/2} in CoMoN_x indicates the Co–N bond, implying the successful synthesis of cobalt nitride [30]. As shown in Fig. 3b, CoMo(OH)_x demonstrated two peaks at 231.3 and 234.5 eV, assigned to Mo 3d_{5/2} and Mo 3d_{3/2} of Mo⁶⁺ in the Mo 3d spectrum [39]. While for the CoMoN_x heterostructure, the spectrum could be deconvoluted into Mo⁴⁺ and Mo⁶⁺, indicating the presence of Mo oxides on the surface of CoMoN_x [40]. In addition, the peak at 229.7 eV corresponds to the Mo–N bond, which is beneficial to improving the HER activity [41]. Moreover, the high valence state of Mo is beneficial to corrosion resistance and intermediate adsorption during water dissociation [42]. As revealed in Fig. 3c, the N 1 s spectrum contains four peaks at 394.4, 396.4, 398.4 and 400.0 eV, corresponding to Mo–N, Co–N, pyridinic N and pyrrolic N, respectively [43–46]. For the high-resolution spectrum of O 1 s for CoMoN_x (Fig. 3d), the peaks located at 529.5, 530.6, and 532.2 eV are ascribed to metal–oxygen (M–O) bonds, carbon–oxygen (C–O), and adsorbed water molecules (H₂O_{ads}), respectively due to the catalyst oxidation in the air [47,48].

3.3. Electrocatalytic HER analysis

The catalytic performance of CoMoN_x heterostructures was evaluated through hydrogen evolution reaction (HER) measurements in a three-electrode system with a 1.0 M KOH solution. The results, as displayed in Fig. 4a–b, showed that the CoMoN_x heterostructures provided lower overpotentials at current densities of 10, 50, and 100 mA cm^{−2}, with values of 44, 101, and 145 mV respectively. Notably, CoMoN_x outperformed Pt/C when the current density exceeded 50 mA cm^{−2}, because its unique nanosheet structure was conducive to electrolyte diffusion and gas release [49]. This indicates that the CoMoN_x heterostructures have a higher efficiency in the HER process. At high current density, the polarization curves fluctuate because of the effect of rapidly generated hydrogen bubbles on the connection between the electrode surface and the electrolyte. Additionally, the CoMoN_x heterostructures showed a low Tafel slope of 55.6 mV dec^{−1}, which is significantly lower compared to other catalysts such as ZIF-67 (110.2 mV dec^{−1}), CoMo(OH)_x (157.3 mV dec^{−1}), and Co_{5.47}N (170.0 mV dec^{−1}). This low Tafel slope is also relatively close to that of Pt/C (27.9 mV dec^{−1}) (Fig. 4c),

indicating that the CoMoN_x heterostructures have a favorable reaction kinetics and follow a Volmer-Heyrovsky mechanism [50]. Furthermore, the results of the electrochemical impedance spectroscopy (EIS) on the CoMoN_x heterostructures showed the smallest charge transfer resistance (R_{ct}), revealing improved interfacial electron transfer (Fig. 4e). This supports the conclusion that the CoMoN_x heterostructures have a high efficiency in the HER process. A comparison between the CoMoN_x heterostructures and other recently reported high-performance catalysts (Fig. 4d and Table S2) showed that the CoMoN_x heterostructures have a lower overpotential and Tafel slope, further emphasizing their superiority in terms of catalytic performance. Overall, the results of the HER measurements provide strong evidence that the CoMoN_x heterostructures have exceptional catalytic properties, making them a promising candidate for various electrochemical applications.

Electrochemical measurements were used to calculate the electrochemical double-layer capacitance (C_{dl}) in the non-faradaic region at different scan rates (Fig. S7). As shown in Fig. 4f, the CoMoN_x reveals the maximum C_{dl} (51.8 mF cm^{−2}). Meanwhile, the electrochemically active surface area (ECSA) was estimated based on the corresponding C_{dl}. Remarkably, CoMoN_x has the highest ECSA (863 cm²), exceeding those of the ZIF-67 (80 cm²), CoMo(OH)_x (410 cm²) and Co_{5.47}N (248 cm²), which manifests that the more active sites are exposed at the heterostructure [21,51]. Besides, the CoMoN_x exhibits the highest specific catalytic activity after normalization by ECSA (Fig. 4g), indicating high inherent activity [52]. The turnover frequency (TOF) calculated from the ICP results was used to evaluate further catalysts' intrinsic activity (Table S1). As seen in Fig. 4h, the same trend was observed for the inherent performance measured through TOFs, where the CoMoN_x possesses the highest TOF at different overpotentials compared to other systems, clearly indicating its excellent intrinsic activity.

In addition to catalytic activity, stability is a crucial indicator for evaluating electrocatalysts in practical applications. The durability of CoMoN_x was measured by cyclic voltammetry and chronopotentiometry. As presented in Fig. 4i, the potential increase is inappreciable after 3000 cycles, revealing the superior cycling stability of CoMoN_x. Additionally, the potential hardly drops over 100 h under a current density of 10 mA cm^{−2}, attesting to excellent long-term galvanostatic stability of CoMoN_x. Additionally, the overpotential increased by only 10 mV after running for 36 h at a current density of 50 mA cm^{−2}. To further assess the morphology and chemical composition change, the post-HER catalyst was inspected by SEM and XPS. The negligible variation of morphology and chemical state verifies the outstanding robustness of CoMoN_x (Figs. S8–S9).

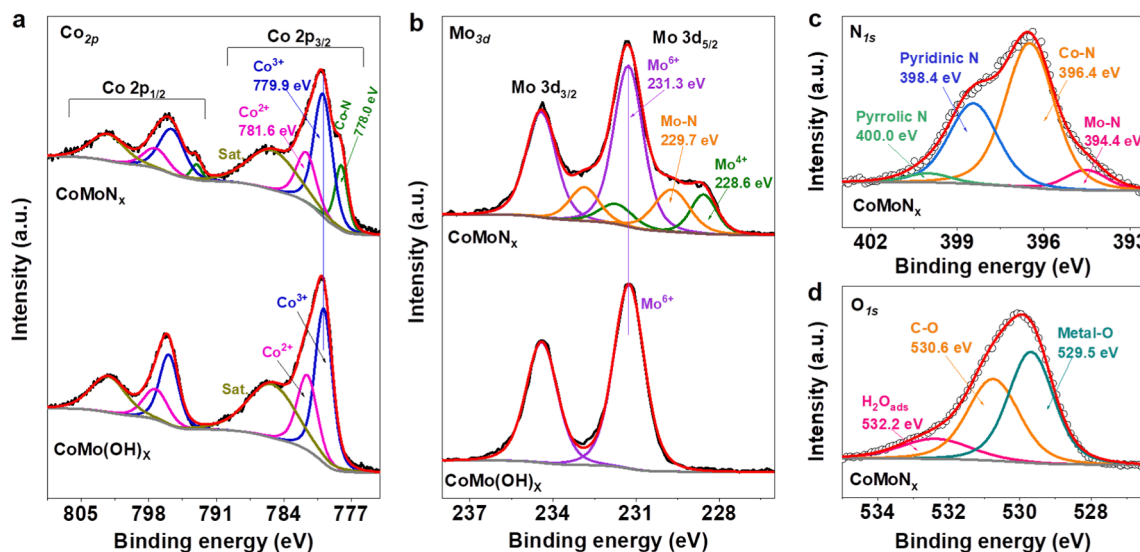


Fig. 3. High-resolution XPS spectra of (a) Co 2p and (b) Mo 3d regions from CoMo(OH)_x and CoMoN_x, respectively; (c) N 1 s and (d) O 1 s regions from CoMoN_x.

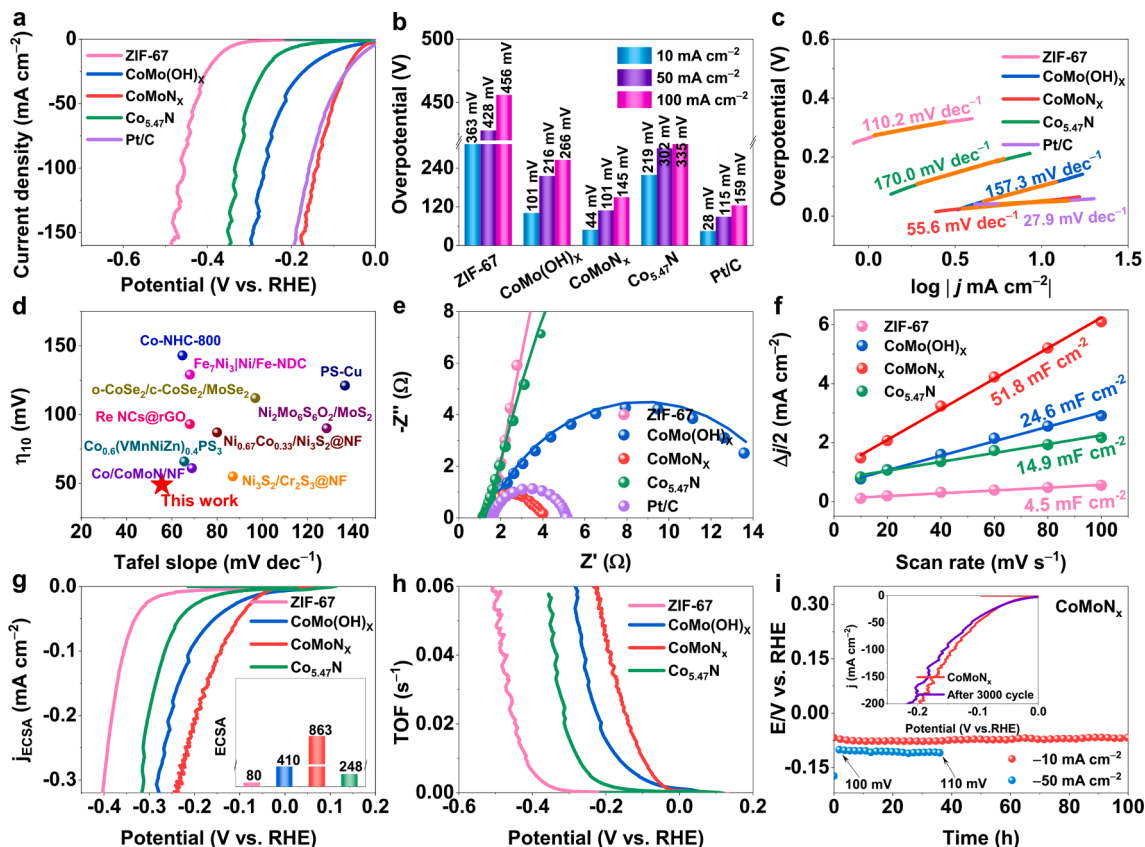


Fig. 4. Electrocatalytic HER performance. (a) LSV polarization curves, (b) comparison of overpotentials at 10, 50 and 100 mA cm⁻², (c) Tafel slopes, (d) comparison of CoMoN_x with previously reported catalysts on an overpotential of -10 mA cm⁻² and Tafel slope, (e) electrochemical impedance spectroscopy (EIS), (f) double-layer capacitance (C_{dl}) plots, (g) ECSA-normalized LSV curves (Inset: bar chart of the ECSA), (h) turnover frequency (TOF) value of ZIF-67, CoMo(OH)_x, CoMoN_x, Co_{5.47}N and Pt/C, (i) durability test of CoMoN_x for HER at -10 and -50 mA cm⁻² (Inset: Polarization curves before and after 3000 cycles of CV curves in 1.0 M KOH solution).

3.4. DFT calculation

Density functional theory (DFT) calculations were used to elucidate further the correlation between the HER performance and interfacial interactions of the heterostructured Co_{5.47}N-Mo₅N₆ catalyst in an alkaline electrolyte. As shown in Fig. S10, correlative theoretical models are constructed to simulate the Co_{5.47}N, Mo₅N₆ and Co_{5.47}N-Mo₅N₆ catalysts. Fig. 5a shows the charge density difference of Co_{5.47}N-Mo₅N₆. It can be found that the electrons are redistributed after forming the interface structure, and a large number of electrons gather at the interface of Co_{5.47}N and Mo₅N₆, indicating that there is a strong interaction between Co_{5.47}N and Mo₅N₆ [53], which is conducive to water splitting. Subsequently, the density of states (DOS) was calculated to elucidate the electronic structure. Compared with Co_{5.47}N and Mo₅N₆, the DOS near the Fermi level of Co_{5.47}N-Mo₅N₆ is higher, indicating that the interaction of Co_{5.47}N and Mo₅N₆ enhances the interfacial conductivity [20], which is expected to improve the adsorption performance and reactivity during HER process. Besides, the *d*-band center of a catalyst is also calculated from their *d*-orbital density of states, and the value of ϵ_d is related to the metal-adsorbate interaction [54]. In Fig. 5b, the ϵ_d of Co_{5.47}N-Mo₅N₆ is -1.16 eV, which is closer to the Fermi level than those of Co_{5.47}N (-1.46 eV) and Mo₅N₆ (-1.80 eV), implying that the Co_{5.47}N-Mo₅N₆ electrocatalyst exhibits an improved electroactivity owing to the moderate adsorption and desorption effect toward the intermediate products [55]. Moreover, the partial state densities of 3*d* orbitals of Co and 4*d* orbitals of Mo on Co_{5.47}N-Mo₅N₆ are shown in Fig. S11. The Co-3*d* and Mo-4*d* orbitals are found to shift slightly downward after forming the interfacial structure, indicating their higher surface activity [21,56].

The free energy diagram and reaction pathways were further calculated to thoroughly investigate the intrinsic mechanism of the heterostructured Co_{5.47}N-Mo₅N₆ catalyst in alkaline HER catalysis. The corresponding adsorption and dissociation configurations of water on Co_{5.47}N-Mo₅N₆, Co_{5.47}N and Mo₅N₆ are included in Fig. S12. Specifically, the rate-determining step is the activation of the H₂O molecule in the transition state (TS), or the rate-determining step is Volmer step (H₂O + e⁻ + * → H* + OH⁻) [57,58]. The water dissociation barrier of Co_{5.47}N-Mo₅N₆ is only 1.36 eV, lower than that of Co_{5.47}N (1.62 eV) and Mo₅N₆ (1.65 eV), implying that the interaction of Co_{5.47}N and Mo₅N₆ can significantly reduce the water dissociation energy barrier, accelerate the dissociation kinetics of H₂O, and enhance the generation of H* atoms [59]. All these results contribute to the fast kinetics of HER. Subsequently, in the Heyrovsky step of Fig. 5c, the Co_{5.47}N-Mo₅N₆ surface (0.10 eV) exhibits a more suitable hydrogen binding energy (ΔG_{H^*}), which is closer to zero compared to that on the Co_{5.47}N (-0.63 eV) and Mo₅N₆ (0.16 eV) surfaces, indicating that the Co_{5.47}N-Mo₅N₆ heterocatalyst has the optimal hydrogen adsorption/desorption capacity [53]. Based on experimental and theoretical results, an alkaline HER mechanism on Co_{5.47}N-Mo₅N₆ heterostructures is proposed in Fig. 5d. Water dissociation readily occurs on the Mo₅N₆ to generate H* (H₂O + e⁻ → H* + OH⁻), and the H* adsorption and desorption easily take place on the Co_{5.47}N-Mo₅N₆ interface (H* → 1/2 H₂). The optimized adsorption/desorption of H* intermediate on the Co_{5.47}N-Mo₅N₆ is critical in promoting the HER activity.

3.5. Overall water splitting analysis

Encouraged by the superior electrochemical activity of CoMoN_x in a

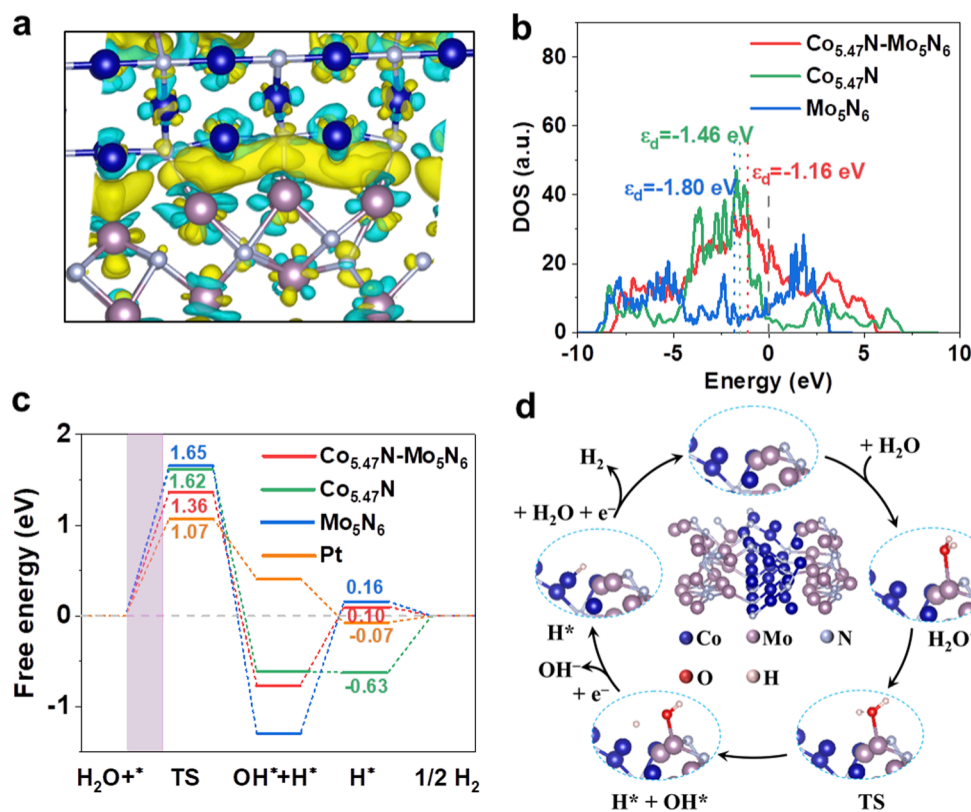


Fig. 5. Density functional theory (DFT) calculations. (a) Schematic diagram of differential charge structure model. The blue, pink and silver balls represent the Co, Mo and N atoms, respectively. (b) Density of states (DOS) of $\text{Co}_{5.47}\text{N}$, Mo_5N_6 and $\text{Co}_{5.47}\text{N-Mo}_5\text{N}_6$. Dotted lines represent the d -band centers of the catalysts. (c) Free energy diagram of water dissociation and H^* adsorption on different catalysts. (d) HER mechanism illustration of $\text{Co}_{5.47}\text{N-Mo}_5\text{N}_6$ in alkaline electrolyte. (For interpretation of the references to color in this figure legend, the reader is referred to the web version of this article.)

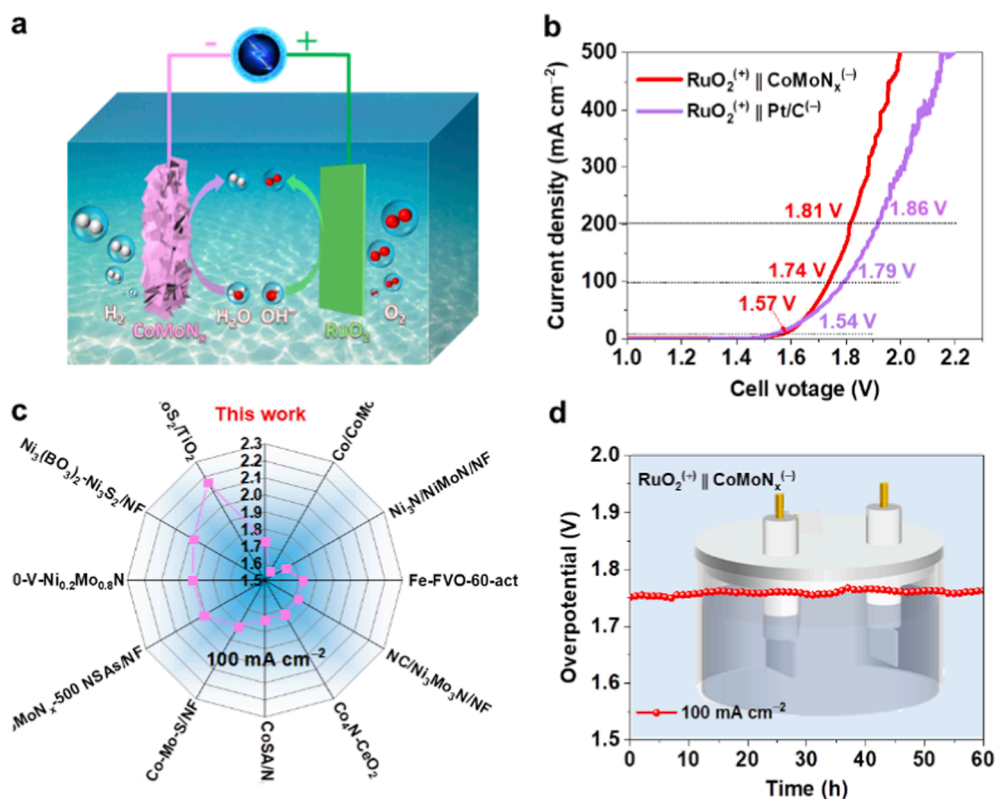


Fig. 6. (a) Schematic diagram of overall water splitting for the two-electrode system, (b) LSV curves of overall water splitting for $\text{CoMoN}_x^{(-)}||\text{RuO}_2^{(+)}$ and $\text{Pt/C}^{(-)}||\text{RuO}_2^{(+)}$, (c) comparison of the cell voltage of CoMoN_x at 100 mA cm^{-2} with previously reported catalysts, and (d) chronopotentiometry test at 100 mA cm^{-2} .

three-electrode cell, a two-electrode device was fabricated using CoMoN_x and RuO₂ as the respective cathode and anode to appraise the feasibility of overall water splitting (CoMoN_x⁽⁻⁾||RuO₂⁽⁺⁾, Fig. 6a). As displayed in Fig. 6b, the CoMoN_x⁽⁻⁾||RuO₂⁽⁺⁾ system only required lower cell voltages of 1.74 V and 1.81 V to reach the current densities of 100 and 200 mA cm⁻², respectively, outperforming the Pt/C⁽⁻⁾||RuO₂⁽⁺⁾ system (1.79 V and 1.86 V). The overall water-splitting performance of the CoMoN_x-based system is superior to most recently reported electrocatalysts (Fig. 6c and Table S3). As shown in Fig. 6d, the chronopotentiometry curve of the CoMoN_x⁽⁻⁾||RuO₂⁽⁺⁾ system displays a negligible degradation after continuous operation at 100 mA cm⁻² for 60 h, verifying the excellent stability of CoMoN_x during the water splitting.

As discussed above, the superior HER performance of CoMoN_x can be attributed to the following aspects: (1) The as-prepared self-supporting binder-free electrodes reduce electrode resistance and accelerate charge transfer, thereby facilitating electrode reactions. (2) The particular structure of ultrathin porous nanosheets is conducive to exposing plentiful active sites and accelerating the charge transfer, thereby facilitating the electrode reaction. (3) DFT calculations reveal that the strong synergy at the interface of Co_{0.5}47N and Mo₅N₆ reduces the water dissociation energy barrier and accelerates the dissociation of water molecules to generate H*, thereby enhancing the HER activity.

4. Conclusion

In summary, the preparation of a sheet-like CoMoN_x hybrid catalyst on carbon cloth using a facile method was investigated for its potential in hydrogen evolution reaction and overall water splitting. The results showed that the ultra-thin nanosheets with a rich interface between Co_{0.5}47N and Mo₅N₆ can expose more active sites and accelerate charge transfer. This unique bimetallic composite structure also reduced the energy barrier for water dissociation and optimized the hydrogen-adsorption free energy. Consequently, the prepared CoMoN_x catalyst exhibited prominent HER catalytic capability with an ultralow overpotential of 44 mV at 10 mA cm⁻², which outperformed most reported transition metal nitrides. Additionally, the overall water splitting test with the CoMoN_x as the cathode produced a cell voltage of 1.57 V at 10 mA cm⁻², a superior performance compared to most recently reported catalysts. This study provides a new and cost-effective strategy for the preparation of bimetallic nitride nanosheet catalysts for hydrogen evolution reactions.

CRedit authorship contribution statement

Yan Hu: Conceptualization, Data curation, Formal analysis, Investigation, Writing - original draft. **Zhiyang Huang:** Investigation, Data curation, Formal analysis. **Qing Zhang:** Data curation, Conceptualization. **Tayirjan Taylor Isimjan:** Investigation, Methodology. **Youqi Chu:** Data curation, Conceptualization. **Yongbiao Mu:** Data curation, Conceptualization. **Baoxin Wu:** Investigation, Methodology. **Zebing Huang:** Investigation, Methodology. **Xiulin Yang:** Supervision, Funding acquisition, Writing - review & editing. **Lin Zeng:** Funding acquisition, Methodology, Supervision, Writing - review & editing.

Declaration of Competing Interest

The authors declare that they have no known competing financial interests or personal relationships that could have appeared to influence the work reported in this paper.

Data availability

The authors do not have permission to share data.

Acknowledgements

This work has been supported by the National Natural Science Foundation of China (no. 21965005), Natural Science Foundation of Guangxi Province (2021GXNSFAA076001), Shenzhen Fundamental Research Programs (JCYJ20200109141216566), Guangdong Basic and Applied Basic Research Foundation (No.2022B1515120004), Project of High-Level Talents of Guangxi (F-KA18015), and Guangxi Technology Base and Talent Subject (GUIKE AD18126001, GUIKE AD20297039). The authors would also like to acknowledge the technical support from SUSTech Core Research Facilities.

Appendix A. Supplementary material

Supplementary data to this article can be found online at <https://doi.org/10.1016/j.jcis.2023.04.028>.

References

- [1] I.S. Kwon, I.H. Kwak, G.M. Zewdie, S.J. Lee, J.Y. Kim, S.J. Yoo, J.-G. Kim, J. Park, H.S. Kang, MoSe₂-VSe₂-NbSe₂ ternary alloy nanosheets to boost electrocatalytic hydrogen evolution reaction, *Adv. Mater.* 34 (2022) 2205524, <https://doi.org/10.1002/adma.202205524>.
- [2] Y. Liu, Y. Chen, Y. Tian, T. Sakthivel, H. Liu, S. Guo, H. Zeng, Z. Dai, Synergizing hydrogen spillover and deprotonation by the internal polarization field in a MoS₂/NiPS₃ vertical heterostructure for boosted water electrolysis, *Adv. Mater.* 34 (2022) 2203615, <https://doi.org/10.1002/adma.202203615>.
- [3] Y.-C. Zhang, C. Han, J. Gao, L. Pan, J. Wu, X.-D. Zhu, J.-J. Zou, NiCo-based electrocatalysts for the alkaline oxygen evolution reaction: a review, *ACS Catal.* 11 (2021) 12485–12509, <https://doi.org/10.1021/acscatal.1c03260>.
- [4] C. Wang, A. Schechter, L. Feng, Iridium-based catalysts for oxygen evolution reaction in acidic media: mechanism, catalytic promotion effects and recent progress, *Nano Res. Energy* (2023), <https://doi.org/10.26599/NRE.2023.9120056>.
- [5] Z. Huang, Z. Liu, M. Liao, L. Wang, Z. Luo, T.T. Isimjan, X. Yang, Synergistically improved hydrogen evolution by interface engineering of monodispersed Co_{0.5}47N/CoMoO₄ hybrid particles on carbon cloth with rich oxygen vacancies, *Chem. Eng. J.* 462 (2023) 142281, <https://doi.org/10.1016/j.cej.2023.142281>.
- [6] X.-D. Zhu, Y. Xie, Y.-T. Liu, Exploring the synergy of 2D MXene-supported black phosphorus quantum dots in hydrogen and oxygen evolution reactions, *J. Mater. Chem. A* 6 (2018) 21255–21260, <https://doi.org/10.1039/C8TA08374F>.
- [7] L.-L. Gu, J. Gao, S.-Y. Qiu, K.-X. Wang, C. Wang, K.-N. Sun, X.-D. Zhu, Prussian-blue-derived FeS₂ spheres with abundant pore canals for efficient hydrogen evolution reaction, *Chem. Eng. Sci.* 262 (2022), 118028, <https://doi.org/10.1016/j.ces.2022.118028>.
- [8] C. Li, Z. Wang, M. Liu, E. Wang, B. Wang, L. Xu, K. Jiang, S. Fan, Y. Sun, J. Li, K. Liu, Ultrafast self-heating synthesis of robust heterogeneous nanocarbitides for high current density hydrogen evolution reaction, *Nat. Commun.* 13 (2022) 3338, <https://doi.org/10.1038/s41467-022-31077-x>.
- [9] W. Tang, S. Zhu, H. Jiang, Y. Liang, Z. Li, S. Wu, Z. Cui, Self-supporting nanoporous CoMoP electrocatalyst for hydrogen evolution reaction in alkaline solution, *J. Colloid Interface Sci.* 625 (2022) 606–613, <https://doi.org/10.1016/j.jcis.2022.06.085>.
- [10] Z. Luo, Q. Peng, Z. Huang, L. Wang, Y. Yang, J. Dong, T.T. Isimjan, X. Yang, Fine-tune d-band center of cobalt vanadium oxide nanosheets by N-doping as a robust overall water splitting electrocatalyst, *J. Colloid Interface Sci.* 629 (2023) 111–120, <https://doi.org/10.1016/j.jcis.2022.09.069>.
- [11] H. Tan, B. Tang, Y. Lu, Q. Ji, L. Lv, H. Duan, N. Li, Y. Wang, S. Feng, Z. Li, C. Wang, F. Hu, Z. Sun, W. Yan, Engineering a local acid-like environment in alkaline medium for efficient hydrogen evolution reaction, *Nat. Commun.* 13 (2022) 2024, <https://doi.org/10.1038/s41467-022-29710-w>.
- [12] Y. Hu, Z. Luo, M. Guo, J. Dong, P. Yan, C. Hu, T.T. Isimjan, X. Yang, Interface engineering of Co₂N_{0.67}/CoMoO₄ heterostructure nanosheets as a highly active electrocatalyst for overall water splitting and Zn-H₂O cell, *Chem. Eng. J.* 435 (2022), 134795, <https://doi.org/10.1016/j.cej.2022.134795>.
- [13] Q. Yu, Z. Zhang, S. Qiu, Y. Luo, Z. Liu, F. Yang, H. Liu, S. Ge, X. Zou, B. Ding, W. Ren, H.-M. Cheng, C. Sun, B. Liu, A Ta-TaS₂ monolith catalyst with robust and metallic interface for superior hydrogen evolution, *Nat. Commun.* 12 (2021) 6051, <https://doi.org/10.1038/s41467-021-26315-7>.
- [14] Y. Liu, J. Wu, K.P. Hackenberg, J. Zhang, Y.M. Wang, Y. Yang, K. Keyshar, J. Gu, T. Ogitsu, R. Vajtai, J. Lou, P.M. Ajayan, Brandon C. Wood, B.I. Yakobson, Self-optimizing, highly surface-active layered metal dichalcogenide catalysts for hydrogen evolution, *Nat. Energy* 2 (2017) 17127, <https://doi.org/10.1038/nenergy.2017.127>.
- [15] Z. Yang, C. Zhao, Y. Qu, H. Zhou, F. Zhou, J. Wang, Y. Wu, Y. Li, Trifunctional self-supporting cobalt-embedded carbon nanotube films for ORR, OER, and HER triggered by solid diffusion from bulk metal, *Adv. Mater.* 31 (2019) 1808043, <https://doi.org/10.1002/adma.201808043>.
- [16] K. Dai, N. Zhang, L. Zhang, L. Yin, Y. Zhao, B. Zhang, Self-supported Co/CoO anchored on N-doped carbon composite as bifunctional electrocatalyst for efficient

- overall water splitting, *Chem. Eng. J.* 414 (2021), 128804, <https://doi.org/10.1016/j.cej.2021.128804>.
- [17] X. Huang, X. Xu, X. Luan, D. Cheng, CoP nanowires coupled with CoMoP nanosheets as a highly efficient cooperative catalyst for hydrogen evolution reaction, *Nano Energy* 68 (2020), 104332, <https://doi.org/10.1016/j.nanoen.2019.104332>.
- [18] P. Wang, R. Qin, P. Ji, Z. Pu, J. Zhu, C. Lin, Y. Zhao, H. Tang, W. Li, S. Mu, Synergistic coupling of Ni nanoparticles with Ni₃C nanosheets for highly efficient overall water splitting, *Small* 16 (2020) 2001642, <https://doi.org/10.1002/sml.202001642>.
- [19] Y. Liu, B. Zhou, Y. Zhang, W. Xiao, B. Li, Z. Wu, L. Wang, In situ synthesis of two-dimensional graphene-like nickel-molybdenum nitride as efficient electrocatalyst towards water-splitting under large-current density, *J. Colloid Interface Sci.* 637 (2023) 104–111, <https://doi.org/10.1016/j.jcis.2023.01.069>.
- [20] F. Lin, Z. Dong, Y. Yao, L. Yang, F. Fang, L. Jiao, Electrocatalytic hydrogen evolution of ultrathin Co-Mo₅N₆ heterojunction with interfacial electron redistribution, *Adv. Energy Mater.* 10 (2020) 2002176, <https://doi.org/10.1002/aenm.202002176>.
- [21] H. Ma, Z. Chen, Z. Wang, C.V. Singh, Q. Jiang, Interface engineering of Co/CoMoN/NF heterostructures for high-performance electrochemical overall water splitting, *Adv. Sci.* 9 (2022) 2105313, <https://doi.org/10.1002/advs.202105313>.
- [22] P. Yan, M. Huang, B. Wang, Z. Wan, M. Qian, H. Yan, T.T. Isimjan, J. Tian, X. Yang, Oxygen defect-rich double-layer hierarchical porous Co₃O₄ arrays as high-efficient oxygen evolution catalyst for overall water splitting, *J. Energy Chem.* 47 (2020) 299–306, <https://doi.org/10.1016/j.jechem.2020.02.006>.
- [23] W. Liu, Z. Xiao, S. Chandrasekaran, D. Fan, W. Li, H. Lu, Y. Liu, Insights into the effect of sulfur incorporation into tungsten diphosphide for improved hydrogen evolution reaction, *ACS Appl. Mater. Interfaces* 14 (2022) 16157–16164, <https://doi.org/10.1021/acscami.1c24363>.
- [24] P. Yan, Y. Qin, Y. Yang, X. Shao, T.T. Isimjan, X. Yang, Controllable transformation of sheet-like CoMo-hydro(oxide) and phosphide arrays on nickel foam as efficient catalysts for alkali water splitting and Zn–H₂O cell, *Int. J. Hydrog. Energy* 47 (2022) 23530–23539, <https://doi.org/10.1016/j.ijhydene.2022.05.136>.
- [25] J. Cao, T. Li, H. Gao, Y. Lin, X. Wang, H. Wang, T. Palacios, X. Ling, Realization of 2D crystalline metal nitrides via selective atomic substitution, *Sci. Adv.* 6 (2020) eaax8784, <https://doi.org/10.1126/sciadv.aax8784>.
- [26] T. Liu, Y. Tian, M. Li, Z. Su, J. Bai, C. Ma, X. Bo, W. Guan, M. Zhou, Insight into a class of cobalt nitrides for oxygen evolution catalysis: nitrogen-rich matters, *Electrochim. Acta* 323 (2019), 134684, <https://doi.org/10.1016/j.electacta.2019.134684>.
- [27] X.-Z. Song, N. Zhang, F. Liu, Z.-H. Wang, W.-Y. Zhu, G.-Z. Zhang, Z.-Y. Niu, X.-F. Wang, Z. Tan, Spontaneously engineering heterogeneous interface of silver nanoparticles on α -Co(OH)₂ for boosting electrochemical oxygen evolution, *J. Alloys Compd.* 873 (2021), 159766, <https://doi.org/10.1016/j.jallcom.2021.159766>.
- [28] W. Jiang, J. Chen, G. Qian, H. He, H. Zhang, X. Zhuo, F. Shen, L. Luo, S. Yin, Interfacial electronic engineering of carbon encapsulated Co_{5.47}N-WO₃ for boosting overall water splitting, *Electrochim. Acta* 390 (2021) 138887, <https://doi.org/10.1016/j.electacta.2021.138887>.
- [29] Z. Wang, G. Qian, T. Yu, J. Chen, F. Shen, L. Luo, Y. Zou, S. Yin, Carbon encapsulated FeWO₄-Ni₃S₂ nanosheets as a highly active catalyst for overall water splitting at large current density, *Chem. Eng. J.* 434 (2022), 134669, <https://doi.org/10.1016/j.cej.2022.134669>.
- [30] Q. Qian, J. Zhang, J. Li, Y. Li, X. Jin, Y. Zhu, Y. Liu, Z. Li, A. El-Harairy, C. Xiao, G. Zhang, Y. Xie, Artificial heterointerfaces achieve delicate reaction kinetics towards hydrogen evolution and hydrazine oxidation catalysis, *Angew. Chem. Int. Ed.* 60 (2021) 5984–5993, <https://doi.org/10.1002/anie.202014362>.
- [31] J. Diao, Y. Qiu, S. Liu, W. Wang, K. Chen, H. Li, W. Yuan, Y. Qu, X. Guo, Interfacial engineering of W₂N/WC heterostructures derived from solid-state synthesis: a highly efficient trifunctional electrocatalyst for ORR, OER, and HER, *Adv. Mater.* 32 (2020) 1905679, <https://doi.org/10.1002/adma.201905679>.
- [32] H. Zhang, D. Tian, Z. Zhao, X. Liu, Y.-N. Hou, Y. Tang, J. Liang, Z. Zhang, X. Wang, J. Qiu, Cobalt nitride nanoparticles embedded in porous carbon nanosheet arrays propelling polysulfides conversion for highly stable lithium–sulfur batteries, *Energy Stor. Mater.* 21 (2019) 210–218, <https://doi.org/10.1016/j.ensm.2018.12.005>.
- [33] T. Xiong, X. Yao, Z. Zhu, R. Xiao, Y.-W. Hu, Y. Huang, S. Zhang, M.S. Balogun, In situ grown Co-based interstitial compounds: non-3d metal and non-metal dual modulation boosts alkaline and acidic hydrogen electrocatalysis, *Small* 18 (2022) 2105331, <https://doi.org/10.1002/sml.202105331>.
- [34] V.K. Singh, U.T. Nakate, P. Bhuyan, J. Chen, D.T. Tran, S. Park, Mo/Co doped 1T-VS₂ nanostructures as a superior bifunctional electrocatalyst for overall water splitting in alkaline media, *J. Mater. Chem. A* 10 (2022) 9067–9079, <https://doi.org/10.1039/D2TA00488G>.
- [35] J. Lin, Y. Yan, T. Xu, J. Cao, X. Zheng, J. Feng, J. Qi, Rich P vacancies modulate Ni₂P/Cu₃P interfaced nanosheets for electrocatalytic alkaline water splitting, *J. Colloid Interface Sci.* 564 (2020) 37–42, <https://doi.org/10.1016/j.jcis.2019.12.114>.
- [36] Y. Yang, Y. Huang, S. Zhou, Y. Liu, L. Shi, T.T. Isimjan, X. Yang, Delicate surface vacancies engineering of Ru doped MOF-derived Ni-NiO@C hollow microsphere superstructure to achieve outstanding hydrogen oxidation performance, *J. Energy Chem.* 72 (2022) 395–404, <https://doi.org/10.1016/j.jechem.2022.06.011>.
- [37] X. Ma, W. Zhao, Q. Deng, X. Fu, L. Wu, W. Yan, Y. Yang, In-situ construction of Cu–Co₄N@CC hierarchical binder-free cathode for advanced and flexible Li–CO₂ batteries: electron structure and mass transfer modulation, *J. Power Sources* 535 (2022), 231446, <https://doi.org/10.1016/j.jpowsour.2022.231446>.
- [38] C. Wang, F. Wang, S.-Y. Qiu, J. Gao, L.-L. Gu, K.-X. Wang, P.-J. Zuo, K.-N. Sun, X.-D. Zhu, Integrating Co₃O₄ nanoparticles with MnO₂ nanosheets as bifunctional electrocatalysts for water splitting, *Int. J. Hydrog. Energy* 46 (2021) 10356–10365, <https://doi.org/10.1016/j.ijhydene.2020.12.134>.
- [39] X. Mao, Y. Wang, C. Xiang, D. Zhan, H. Zhang, E. Yan, F. Xu, X. Hu, J. Zhang, L. Sun, Y. Zou, Core-shell structured CuCo₂S₄@CoMoO₄ nanorods for advanced electrode materials, *J. Alloys Compd.* 844 (2020), 156133, <https://doi.org/10.1016/j.jallcom.2020.156133>.
- [40] A. Saad, Y. Gao, K.A. Owusu, W. Liu, Y. Wu, A. Ramiere, H. Guo, P. Tsiakaras, X. Cai, Ternary Mo₂NiB₂ as a superior bifunctional electrocatalyst for overall water splitting, *Small* 18 (2022), e2104303, <https://doi.org/10.1002/sml.202104303>.
- [41] W. Xie, T. Yu, Z. Ou, J. Zhang, R. Li, S. Song, Y. Wang, Self-supporting clusters constituted of nitrogen-doped CoMoO₄ nanosheets for efficiently catalyzing the hydrogen evolution reaction in alkaline media, *ACS Sustain. Chem. Eng.* 8 (2020) 9070–9078, <https://doi.org/10.1021/acssuschemeng.0c02283>.
- [42] Y. Chen, J. Yu, J. Jia, F. Liu, Y. Zhang, G. Xiong, R. Zhang, R. Yang, D. Sun, H. Liu, W. Zhou, Metallic Ni₃Mo₃N porous microrods with abundant catalytic sites as efficient electrocatalyst for large current density and superstability of hydrogen evolution reaction and water splitting, *Appl. Catal. B: Environ.* 272 (2020), 118956, <https://doi.org/10.1016/j.apcatb.2020.118956>.
- [43] P. Wang, J. Qi, C. Li, X. Chen, T. Wang, C. Liang, N-doped carbon nanotubes encapsulating ni/mon heterostructures grown on carbon cloth for overall water splitting, *ChemElectroChem* 7 (2020) 745–752, <https://doi.org/10.1002/celec.202000023>.
- [44] Y. Yang, R. Zeng, Y. Xiong, F.J. DiSalvo, H.D. Abruña, Cobalt-based nitride-core oxide-shell oxygen reduction electrocatalysts, *J. Am. Chem. Soc.* 141 (2019) 19241–19245, <https://doi.org/10.1021/jacs.9b10809>.
- [45] Y. Lu, Z. Li, Y. Xu, L. Tang, S. Xu, D. Li, J. Zhu, D. Jiang, Bimetallic Co-Mo nitride nanosheet arrays as high-performance bifunctional electrocatalysts for overall water splitting, *Chem. Eng. J.* 411 (2021), 128433, <https://doi.org/10.1016/j.cej.2021.128433>.
- [46] F. Guo, M. Zhang, S. Yi, X. Li, R. Xin, M. Yang, B. Liu, H. Chen, H. Li, Y. Liu, Metal-coordinated porous polydopamine nanospheres derived Fe₃N-FeCo encapsulated N-doped carbon as a highly efficient electrocatalyst for oxygen reduction reaction, *Nano Res. Energy* 1 (2022) 9120027, <https://doi.org/10.26599/NRE.2022.9120027>.
- [47] K. Shah, R. Dai, M. Mateen, Z. Hassan, Z. Zhuang, C. Liu, M. Israr, W.-C. Cheong, B. Hu, R. Tu, C. Zhang, X. Chen, Q. Peng, C. Chen, Y. Li, Cobalt single atom incorporated in ruthenium oxide sphere: a robust bifunctional electrocatalyst for HER and OER, *Angew. Chem. Int. Ed.* 61 (2021) e202114951, <https://doi.org/10.1002/anie.202114951>.
- [48] X. Zhao, S. Zhao, S. Li, X. Yao, X. Zhu, W. Chen, G. Fan, Z. Liu, Q. Liu, K. Yue, CoO nanotubes loaded on graphene and modified with porphyrin moieties for colorimetric sensing of dopamine, *ACS Appl. Nano Mater.* 4 (2021) 8706–8715, <https://doi.org/10.1021/acsnm.1c01205>.
- [49] M. Guo, A. Qayum, S. Dong, X. Jiao, D. Chen, T. Wang, In situ conversion of metal (Ni, Co or Fe) foams into metal sulfide (Ni₃S₂, Co₉S₈ or FeS) foams with surface grown N-doped carbon nanotube arrays as efficient superaerophobic electrocatalysts for overall water splitting, *J. Mater. Chem. A* 8 (2020) 9239–9247, <https://doi.org/10.1039/D0TA02337J>.
- [50] M. Li, L. Wang, Y. Qian, J. Du, Facile synthesis of MoS₂/CuS nanoflakes as high performance electrocatalysts for hydrogen evolution reaction, *Int. J. Hydrog. Energy* 47 (2022) 5319–5325, <https://doi.org/10.1016/j.ijhydene.2021.11.182>.
- [51] D. Chen, R. Lu, R. Yu, Y. Dai, H. Zhao, D. Wu, P. Wang, J. Zhu, Z. Pu, L. Chen, J. Yu, S. Mu, Work-function-induced interfacial built-in electric fields in Os-OsSe₂ heterostructures for active acidic and alkaline hydrogen evolution, *Angew. Chem. Int. Ed.* 61 (2022), e202208642, <https://doi.org/10.1002/anie.202208642>.
- [52] J.-Y. Zhang, J. Liang, B. Mei, K. Lan, L. Zu, T. Zhao, Y. Ma, Y. Chen, Z. Lv, Y. Yang, C. Yu, Z. Xu, B.Y. Xia, W. Li, Q. Yuan, D. Zhao, Synthesis of Ni/NiO@MoO_{3-x} composite nanoarrays for high current density hydrogen evolution reaction, *Adv. Funct. Mater.* 12 (2022) 2200001, <https://doi.org/10.1002/aenm.202200001>.
- [53] K. Wang, S. Wang, K.S. Hui, H. Gao, D.A. Dinh, C. Yuan, C. Zha, Z. Shao, Z. Tang, K. N. Hui, Synergistically boosting the elementary reactions over multiheterogeneous ordered macroporous Mo₂C/NC-Ru for highly efficient alkaline hydrogen evolution, *Carbon Energy* 4 (2022) 856–866, <https://doi.org/10.1002/cey2.188>.
- [54] X. Liu, S. Zhang, J. Liang, S. Li, H. Shi, J. Liu, T. Wang, J. Han, Q. Li, Protusion-rich Cu@NiRu Core@shell nanotubes for efficient alkaline hydrogen evolution electrocatalysis, *Small* 18 (2022) 2202496, <https://doi.org/10.1002/sml.202202496>.
- [55] L. Gao, Z. Yang, T. Sun, X. Tan, W. Lai, M. Li, J. Kim, Y.-F. Lu, S.-I. Choi, W. Zhang, C. Ma, S.C. Smith, Y.-G. Zhou, H. Huang, Autocatalytic surface reduction-assisted synthesis of ptw ultrathin alloy nanowires for highly efficient hydrogen evolution reaction, *Adv. Funct. Mater.* 12 (2022) 2103943, <https://doi.org/10.1002/aenm.202103943>.
- [56] Z. Zhang, C. Feng, D. Wang, S. Zhou, R. Wang, S. Hu, H. Li, M. Zuo, Y. Kong, J. Bao, J. Zeng, Selectively anchoring single atoms on specific sites of supports for improved oxygen evolution, *Nat. Commun.* 13 (2022) 2473, <https://doi.org/10.1038/s41467-022-30148-3>.
- [57] Q. He, Y. Zhou, H. Shou, X. Wang, P. Zhang, W. Xu, S. Qiao, C. Wu, H. Liu, D. Liu, S. Chen, R. Long, Z. Qi, X. Wu, L. Song, Synergic reaction kinetics over adjacent

- ruthenium sites for superb hydrogen generation in alkaline media, *Adv. Mater.* 34 (2022) 2110604, <https://doi.org/10.1002/adma.202110604>.
- [58] Q. He, D. Tian, H. Jiang, D. Cao, S. Wei, D. Liu, P. Song, Y. Lin, L. Song, Achieving efficient alkaline hydrogen evolution reaction over a Ni₅P₄ catalyst incorporating single-atomic Ru sites, *Adv. Mater.* 32 (2020) 1906972, <https://doi.org/10.1002/adma.201906972>.
- [59] J. Liu, C. Tang, Z. Ke, R. Chen, H. Wang, W. Li, C. Jiang, D. He, G. Wang, X. Xiao, Optimizing hydrogen adsorption by d-d orbital modulation for efficient hydrogen evolution catalysis, *Adv. Funct. Mater.* 12 (2022) 2103301, <https://doi.org/10.1002/aenm.202103301>.